Journal of The Electrochemical Society, **155** (6) B635-B643 (2008)
0013-4651/2008/155(6)/B635/9/$23.00 © The Electrochemical Society

Triple-Phase Boundary and Surface Transport in Mixed Conducting Patterned Electrodes

Matthew E. Lynch,[a] David S. Mebane,[a] Yingjie Liu,[b] and Meilin Liu[a,*,z]

[a]*Center for Innovative Fuel Cell and Battery Technologies, School of Materials Science and Engineering, and* [b]*School of Mathematics, Georgia Institute of Technology, Atlanta, Georgia 30332, USA*

The mathematical framework required to account for a triple-phase boundary (TPB) and the accompanying surface transport was added to a two-dimensional numerical model of a mixed conducting thin film by considering appropriate kinetic rate and mass-transport expressions. Approximate parameters were chosen so that the model qualitatively matched experimental results for patterned $La_{1-x}Sr_xMnO_{3\pm\delta}$ (LSM) electrodes, including trends with respect to thickness, active area, cathodic polarization, and sheet resistance. The rate of the TPB reaction was predicted to decrease due to sheet-resistance limitation, although it is expected to be independent of the active area and thickness of the film electrode when the effect of sheet resistance is insignificant. The addition of this feature is vital to the interpretation of patterned electrode experiments and to precise determination of parameters for better prediction of the electrochemical response of patterned LSM electrodes. The implementation and validation of this model is the next step in the development of continuum models useful to a variety of multiscale investigations of SOFC electrodes.
 [DOI: 10.1149/1.2898152]

Manuscript submitted November 7, 2007; revised manuscript received February 10, 2008. Available electronically May 1, 2008.

Mixed ionic–electronic conducting (MIEC) electrode materials are important in solid oxide fuel cell (SOFC) technology, because their bulk transport pathway extends the reaction zone away from the triple-phase boundary (TPB) and thus increases performance.[1,2] Due to competition between pathways, the various transport and reaction kinetics of these materials are often amalgamated and are difficult to examine individually. To facilitate scientific study, thin film and patterned electrode geometries have been developed to simplify electrode complexity by isolating specific mechanisms. Such experiments[3-24] have yielded valuable information on several candidate fuel cell materials, including $La_{1-x}Sr_xMnO_{3\pm\delta}$ (LSM) and $La_{1-x}Sr_xCoO_{3-\delta}$ (LSC).

Recently, a two-dimensional (2D) numerical model was introduced to describe charge and mass transport in, as well as chemical kinetics on the surface of, a mixed conducting thin film.[25-27] This model provides insight into thin-film electrode response, specifically into the nature of the transport of reactants as well as the effect of sheet resistance. It is potentially useful for making quantitative estimations of phenomenological parameters of electrode materials, directly linking first principles-based calculations to higher levels of modeling, and predicting the performance of thin-film test cells. When decoupled from its rigid geometric framework, the approach has the possibility to be applied onto an arbitrary MIEC geometry.

The purpose of this paper is to extend the model to account for the presence of a TPB and the resulting surface transport. This extension allows greater applicability for a number of multiscale modeling efforts, especially those applied to patterned test cells and to the determination of fundamental material properties. The specific geometry under consideration for development and qualitative validation is shown in Fig. 1 and consists of an array of thin-film MIEC electrodes patterned on top of an electrolyte (Fig. 1a). The model domain (Fig. 1b) is obtained by taking a symmetric 2D cross section from the center of one patterned electrode to the center of the air-exposed electrolyte, separating it from the adjacent electrode. On top of each electrode, a current collector is patterned and covered by an insulator (neither is depicted in Fig. 1a for simplicity). The insulator blocks the TPB at the current collector/MIEC contact and can also selectively block active MIEC surface.[4,14]

In the thin film model, interaction of oxygen with the surface of the MIEC is assumed to involve two elementary steps, dissociative adsorption resulting in partial reduction (Eq. 1) and direct incorporation (Eq. 2)

$$\frac{1}{2}O_2 + s \rightarrow O'_{ads} + h^{\cdot} \quad [1]$$

$$O'_{ads} + V_O^{\cdot\cdot} \rightarrow O_O^x + h^{\cdot} + s \quad [2]$$

where $V_O^{\cdot\cdot}$ represents an oxygen vacancy (in Kröger–Vink notation), s is a surface site, and $h^{\cdot}$ is an electron hole. Each step involves one electron transfer. The oxygen ion incorporated into the MIEC by Reaction 2 is eventually transferred to the electrolyte by exchange with a vacancy across the interface

$$O_{O,m}^x + V_{O,e}^{\cdot\cdot} \rightarrow O_{O,e}^x + V_{O,m}^{\cdot\cdot} \quad [3]$$

where the subscript m signifies that the species is in the MIEC and the subscript e signifies the electrolyte.

Transport in the bulk MIEC is modeled by explicit consideration of oxygen vacancies and electron holes. The governing equations are those regarding the drift-diffusion flux, $\vec{N}_k$, mass conservation, and bulk charge neutrality

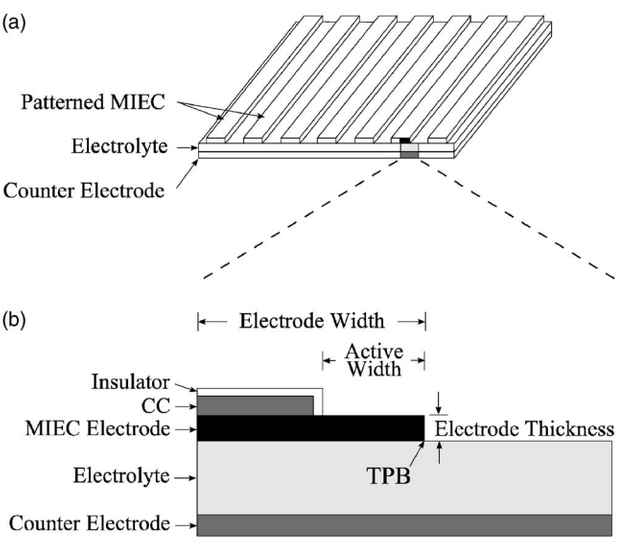

Figure 1. Schematics of (a) patterned electrode array and (b) symmetric 2D cross-sectional model domain. The components of the 2D model domain are indicated by shading where the MIEC is black, the electrolyte is light gray, the current collector and counter electrode are dark gray, and the insulator is white. The current collector and insulator are not indicated in (a) for simplicity.

* Electrochemical Society Active Member.
z E-mail: meilin.liu@mse.gatech.edu

$$\vec{N}_k = -u_k c_k \nabla \tilde{\mu}_k \approx -RTu_k \nabla c_k - z_k F u_k c_k \nabla \phi \quad [4]$$

$$\frac{\partial c_k}{\partial t} = -\nabla \cdot \vec{N}_k + G_k \quad [5]$$

$$F\sum_k z_k c_k + \rho_b = 0 \quad [6]$$

Here, $\tilde{\mu}_k$ is the electrochemical potential of species k (oxygen vacancy or electron hole), c_k is its concentration, z_k is its charge, u_k is its mobility, ϕ is the electrostatic potential, G_k is a homogeneous generation term, ρ_b is the background charge density, R is the universal gas constant, T is the temperature, and F is the Faraday constant.

These equations are discretized according to a conservative finite volume method and solved iteratively to steady state using a line-by-line solver.[25] Kinetic-rate expressions,[26,27] derived to take into account polarization and other relevant electrochemical factors, serve as the boundary conditions. In this paper, the above approach is used as a basis and expanded upon to include the reaction at a TPB as well as surface transport necessitated by such a reaction.

Theory

TPB.— The reaction at the TPB assumes full reduction of adsorbed, partially reduced oxygen and subsequent direct incorporation into the electrolyte

$$O'_{ads} + \ddot{V}_{O,e} \rightarrow O^x_{O,e} + \dot{h}_m + s \quad [7]$$

The kinetic-rate model is similar to those already derived for adsorption, etc. using transition-state theory.[26,27] The electrochemical potential of the initial (I) and final (II) states may be written as the sum of chemical potential (μ) and electrical potential (ϕ) terms

$$\tilde{\mu}^0_{I,tpb} = \mu^0_{O',s} - F\phi_s + \mu^0_{v,e} + 2F\phi_e \quad [8]$$

$$\tilde{\mu}^0_{II,tpb} = \mu^0_{h,m} + F\phi_m \quad [9]$$

where the subscript s represents the surface. Using the transfer coefficient, α, the electrical component (elect.) of the electrochemical potential at transition state A may be expressed as

$$\tilde{\mu}^0_{A,elect.} - \tilde{\mu}^0_{I,elect.} = \alpha(\tilde{\mu}^0_{II,elect.} - \tilde{\mu}^0_{I,elect.}) \quad [10]$$

Substituting the electrical potential components from Eq. 8 and 9 into 10 adding the chemical potential component at state A

$$\tilde{\mu}^0_A = \mu^0_A + F(2\phi_e - \phi_s) + \alpha F(\phi_m + \phi_s - 2\phi_e) \quad [11]$$

After some algebra, the difference in electrochemical potential between states I and A is

$$\begin{aligned}\mu^0_A - \mu^0_I &= \mu^0_A - \mu^0_{O',s} - \mu^0_{v,e} - \alpha F(2\phi_e - \phi_m - \phi_s) \\ &= (\mu^0_A - \mu^0_{O',s} - \mu^0_{v,e}) - \alpha F(\chi_{em} + \chi_{es})\end{aligned} \quad [12]$$

where $\chi_{em} = \phi_e - \phi_m$ and $\chi_{es} = \phi_e - \phi_s$. Also, between states II and A

$$\begin{aligned}\mu^0_A - \mu^0_{II} &= \mu^0_A - \mu^0_{h,m} - F(\alpha - 1)(2\phi_e - \phi_m - \phi_s) \\ &= (\mu^0_A - \mu^0_{h,m}) - F(\alpha - 1)(\chi_{em} + \chi_{es})\end{aligned} \quad [13]$$

The reaction-rate constant k can now be calculated using

$$k = \kappa \frac{k_B T}{h_P} \exp\left(-\frac{\Delta G^0_A}{RT}\right) \quad [14]$$

where κ is the transmission coefficient, k_B and h_P are the well-known Boltzmann and Planck constants, and ΔG^0_A is the standard activation energy for state A. The rate constants of the forward and backward reactions are now given

$$\begin{aligned}\vec{k} &= \vec{\kappa}\frac{k_B T}{h_P}\exp\left(-\frac{\mu^0_A - \mu^0_I}{RT}\right) \\ &= \vec{\kappa}\frac{k_B T}{h_P}\exp\left[-\frac{((\mu^0_A - \mu^0_{O',s} - \mu^0_{v,e}) - \alpha F(\chi_{em} + \chi_{es}))}{RT}\right] \\ &= \vec{k}'\exp\left[\frac{\alpha F(\chi_{em} + \chi_{es})}{RT}\right]\end{aligned} \quad [15]$$

$$\begin{aligned}\overleftarrow{k} &= \overleftarrow{\kappa}\frac{k_B T}{h_P}\exp\left(-\frac{\mu^0_A - \mu^0_{II}}{RT}\right) \\ &= \overleftarrow{\kappa}\frac{k_B T}{h_P}\exp\left\{-\frac{[(\mu^0_A - \mu^0_{h,m}) - F(\alpha - 1)(\chi_{em} + \chi_{es})]}{RT}\right\} \\ &= \overleftarrow{k}'\exp\left[-\frac{(1-\alpha)F(\chi_{em} + \chi_{es})}{RT}\right]\end{aligned} \quad [16]$$

The empirical rate constants $\vec{k}'$ and $\overleftarrow{k}'$ incorporate constant terms in order to simplify. Under the assumption that the reaction is first order and the activity coefficients are constant, the respective reaction rates can be described as follows

$$\vec{r} = \vec{k} \cdot a_{O',s} \cdot a_{v,e} = \vec{k}''\exp\left[\frac{\alpha F(\chi_{em} + \chi_{es})}{RT}\right](\theta)\frac{c_{v,e}}{c_{O,e}} \quad [17]$$

$$\overleftarrow{r} = \overleftarrow{k} \cdot a_s \cdot a_{h,m} = \overleftarrow{k}''\exp\left[-\frac{(1-\alpha)F(\chi_{em} + \chi_{es})}{RT}\right](1-\theta)\frac{c_{h,m}}{c_{Mn,m}} \quad [18]$$

where the fraction of occupied surface sites is θ, $c_{v,e}$, and $c_{O,e}$ signify the concentration of $\ddot{V}_{O,e}$ and regular oxygen lattice sites, respectively, in the electrolyte (in units of mol/m^3), $c_{h,m}$ and $c_{Mn,m}$ signify the concentration of $\dot{h}$ and regular manganese lattice sites, respectively, in the MIEC (in units of mol/m^3), and the empirical rate constants $\vec{k}''$ and $\overleftarrow{k}''$ are related to those developed in Eq. 15 and 16 but incorporate activity coefficients. Setting the forward rate equal to the backward rate leads to the determination of the equilibrium rate constant, k^0_{tpb}

$$\begin{aligned}k^0_{tpb} &= \vec{k}'''\theta_0\frac{c^0_{v,e}}{c_{O,e}}\exp\left[\frac{\alpha F(\chi^0_{em} + \chi^0_{es})}{RT}\right] \\ &= \overleftarrow{k}'''(1-\theta_0)\frac{c^0_{h,m}}{c_{Mn,m}}\exp\left[-\frac{F(1-\alpha)(\chi^0_{em} + \chi^0_{es})}{RT}\right]\end{aligned} \quad [19]$$

where the index 0 signifies the equilibrium value and $\vec{k}'''$ and $\overleftarrow{k}'''$ are empirical rate constant incorporating concentration-normalizing terms with units mol/(m s). Now, solving for $\vec{k}'''$ and $\overleftarrow{k}'''$ and substituting, the complete rate equation is obtained

$$r_{tpb} = k^0_{tpb}\left\{\frac{c_{v,e}}{c^0_{v,e}}\frac{\theta}{\theta_0}\exp\left[\frac{\alpha F(\Delta\chi_{em} + \Delta\chi_{es})}{RT}\right] - \frac{c_{h,m}}{c^0_{h,m}}\frac{1-\theta}{1-\theta_0}\exp\left[-\frac{F(1-\alpha)(\Delta\chi_{em} + \Delta\chi_{es})}{RT}\right]\right\} \quad [20]$$

where $\Delta\chi_{em} = \chi_{em} - \chi^0_{em}$, $\Delta\chi_{es} = \chi_{es} - \chi^0_{es}$, c represents concentration with units of mol/m^3 and r_{tpb} has units mol/(m s). The value of χ_{em} is easily determined by $\phi_e - \phi_m$, but determining χ_{es} is more complicated. Fortunately, the change in potential $\chi_{ms} = \phi_m - \phi_s$ is calculated routinely in other parts of the model (adsorption, incorporation) using a parallel plate capacitor approximation

$$\chi_{ms} = \phi_m - \phi_s \approx \frac{dQ}{A\epsilon_0} = \frac{d(F\Gamma\theta)}{\epsilon_0} \quad [21]$$

where d is the distance of charge separation, Q is the total charge, and A is the area of the plates. Now, χ_{ms} can be used to indirectly calculate χ_{es} with known values

$$\chi_{es} = \phi_e - \phi_s = \phi_e + (-\phi_m + \phi_m) - \phi_s = (\phi_e - \phi_m) + (\phi_m - \phi_s)$$
$$= \chi_{em} + \chi_{ms} = \chi_{em} + \frac{d_{ms}F\Gamma\theta}{\epsilon_0} \quad [22]$$

The equilibrium case follows

$$\chi^0_{es} = (\phi^0_e - \phi^0_m) + (\phi^0_m - \phi^0_s) = \chi^0_{em} + \frac{d_{ms}F\Gamma\theta_0}{\epsilon_0} \quad [23]$$

and now $\Delta\chi_{es}$ may be obtained

$$\Delta\chi_{es} = \chi_{es} - \chi^0_{es}$$
$$= \left(\chi_{em} + \frac{d_{ms}F\Gamma\theta}{\epsilon_0}\right) - \left(\chi^0_{em} + \frac{d_{ms}F\Gamma\theta}{\epsilon_0}\right)$$
$$= \Delta\chi_{em} + \frac{d_{ms}F\Gamma(\theta - \theta_0)}{\epsilon_0} \quad [24]$$

Assuming $\chi^0_{em} = 0$ between the MIEC and electrolyte bulks at equilibrium, then $\Delta\chi_{em} = \chi_{em}$, and Eq. 24 may be simplified accordingly. Now, $\Delta\chi^0_{es}$ may be obtained

$$\Delta\chi^0_{es} = \chi_{es} - \chi^0_{es} = \chi_{em} + \frac{d_{ms}F\Gamma(\theta - \theta_0)}{\epsilon_0}$$
$$= (\phi_e - \phi_m) + \frac{d_{ms}F\Gamma(\theta - \theta_0)}{\epsilon_0} \quad [25]$$

Finally, the TPB reaction rate can be provided with χ_{em} and χ_{es} and taking $\alpha = 1/2$

$$r_{tpb} = k^0_{tpb}\left(\frac{c_{v,e}}{c^0_{v,e}}\frac{\theta}{\theta_0}\exp\left[\frac{F\left(2(\phi_e - \phi_m) + \frac{d_{ms}F\Gamma(\theta - \theta_0)}{\epsilon_0}\right)}{2RT}\right] - \frac{c_{h,m}}{c^0_{h,m}}\frac{1-\theta}{1-\theta_0}\exp\left\{-\frac{F\left[2(\phi_e - \phi_m) + \frac{d_{ms}F\Gamma(\theta - \theta_0)}{\epsilon_0}\right]}{2RT}\right\}\right) \quad [26]$$

Surface transport.— Surface transport is enabled by the consumption of adsorbed oxygen either at the TPB or by nonuniform incorporation into the MIEC, both of which create an electrochemical potential gradient on the surface. A schematic of the discretized domain is given in Fig. 2. The surface cells are indicated just off the surface of the horizontal and vertical faces of the MIEC. The horizontal cells have dimension Δx and the vertical cells have dimension Δy, so the surface cells have dimension either $\Delta g_x = \Delta x$ or $\Delta g_y = \Delta y$, where g simply indicates the surface domain as a way to symbolically set it apart from the bulk.

Equations 4 and 5 are applied in one dimension along the surface

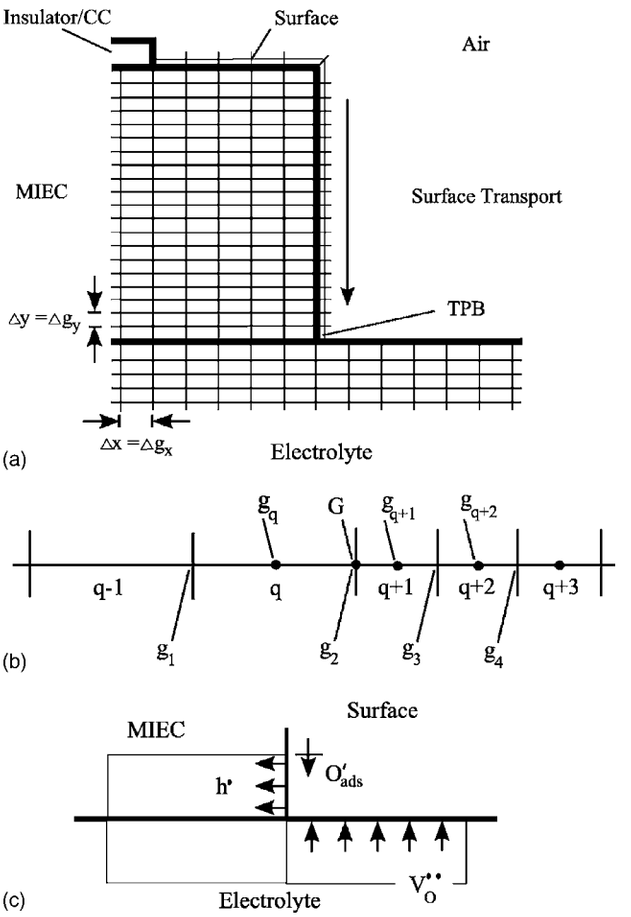

Figure 2. Schematics of (a) 2D finite volume discretization of the surface, MIEC, and electrolyte in the region near the TPB, (b) 1D discretized surface at the corner (straightened) where cell q is the rightmost horizontal surface cell and cell $q + 1$ is the uppermost vertical surface cell, and (c) cells adjacent to the TPB with flow of reactants. Number of cells in (a) and dimension of cells in (a–c) not to scale.

with concentration units of mol/m^2 with the homogeneous generation term, G_k set equal to the difference between the rate of adsorption and the rate of incorporation of oxygen. Thus

$$\frac{\partial c_{O',s}}{\partial t} = -\nabla\cdot(-RTu_{O',s}\nabla c_{O',s} - z_{O',s}Fu_{O',s}c_{O',s}\nabla\phi_s) + (r_{ads} - r_{inc}) \quad [27]$$

$$\Rightarrow \frac{\partial\theta}{\partial t} = -\nabla\cdot(-RTu_{O',s}\nabla\theta - z_{O',s}Fu_{O',s}\theta\nabla\phi_s) + \frac{1}{\Gamma}(r_{ads} - r_{inc}) \quad [28]$$

This equation is discretized over the one-dimensional (1D) surface and solved iteratively to steady state, analogous to the bulk-transport equations.[25] The semidiscrete finite volume expression is

$$\frac{\partial\hat{\theta}}{\partial t} = -\frac{(\hat{M}_{p+1/2} - \hat{M}_{p-1/2})}{\Delta g} + \frac{(\hat{r}_{ads} - \hat{r}_{inc})}{\Gamma} \quad [29]$$

where $\hat{M}$ is the flux normalized by Γ, the carat indicates the average value, p is a cell index distinct from the indices i and j in the bulk, and Δg indicates either Δg_x or Δg_y depending on whether the cell is in the horizontal or vertical portion of the surface, respectively. Applying the backward Euler time discretization

$$\frac{\hat{\theta}^{n+1} - \hat{\theta}^{n}}{\Delta t} = - \frac{(\hat{M}^{n+1}_{p+1/2} - \hat{M}^{n+1}_{p-1/2})}{\Delta g} + \frac{(\hat{r}^{n+1}_{\text{ads}} - \hat{r}^{n+1}_{\text{inc}})}{\Gamma} \quad [30]$$

The flux across the boundary from cell p to cell $p + 1$ is

$$\hat{M}^{n+1}_{p+1/2} = - RTu_{\text{O}',\text{s}} \frac{(\hat{\theta}^{n+1}_{p+1} - \hat{\theta}^{n+1}_{p})}{\Delta g} - z_{\text{O}',\text{s}} Fu_{\text{O}',\text{s}} \frac{(\hat{\theta}^{n+1}_{p+1} + \hat{\theta}^{n+1}_{p})}{2} \frac{(\hat{\phi}^{n+1}_{\text{s},p+1} - \hat{\phi}^{n+1}_{\text{s},p})}{\Delta g} \quad [31]$$

with $\mathcal{O}(\Delta g_x^2)$ approximation error at the steady state. An analogous formula is used for $\hat{M}^{n+1}_{p-1/2}$.

It is desirable to solve for the entire 1D surface at once, from the boundary at the insulator on the horizontal portion of the surface to the endpoint of the vertical portion at the TPB, while preserving second-order accuracy in space. As a consequence, the horizontal and vertical subdomains must be linked despite the fact that they have different cell sizes (Δg_x and Δg_y, respectively).

There are several existing numerical methods in the electrochemical literature that treat cells of different sizes.[28-30] These methods were developed for the case of exponentially expanding cell size and approach the problem from several angles, including transformation into an equal-cell-size space[29] and direct approximation of the flux by computing the finite difference at some average point within each cell.[28] Unfortunately, the latter approach is only first-order accurate in space.[30] Furthermore, the present problem is restricted to two separate subdomains of regularly spaced cells (determined by the bulk discretization), so no elegant transformation into a more uniform space is possible. Therefore, an alternate approach has been taken for the point where the 1D domain transitions from horizontal to vertical, specifically an adjustment of the definition of $\hat{M}$ to one using recovered polynomials.[31-33]

Let the cell q be the rightmost horizontal surface cell, cell $q + 1$ be the uppermost vertical surface cell, and cells $q - 1$, $q + 2$, and $q + 3$ be those adjacent to q and $q + 1$ (see Fig. 2b, where the corner is straightened for simplicity). Also, let the positions g_q, g_{q+1} and g_{q+2} be located at the geometric center of their respective cells and assume that the average concentration of the cell, $\hat{\theta}$, corresponds to its geometric center. Let position g_1 be at the boundary between cells $q - 1$ and q, $g_2 = G$ be at the boundary between cells q and $q + 1$, g_3 be at the boundary between cells $q + 1$ and $q + 2$, and g_4 be at the boundary between cells $q + 2$ and $q + 3$.

Let the function $f(x)$ be defined as the integral of θ from g_1 to some point x along the surface such that

$$f(x) = \int_{g_1}^{x} \theta dg \quad [32]$$

Then, because $\hat{\theta}$ represents the average cell value, $f(g_1) = f_1 = 0$, $f(g_2) = f_2 = \hat{\theta}_q \Delta g_x$, $f(g_3) = f_3 = \hat{\theta}_q \Delta g_x + \hat{\theta}_{q+1} \Delta g_y$, and $f(g_4) = f_4 = \hat{\theta}_q \Delta g_x + \hat{\theta}_{q+1} \Delta g_y + \hat{\theta}_{q+2} \Delta g_y$. Now, using Lagrangian basis functions to define a cubic polynomial, $\beta(g)$, the function f can be interpolated to fourth-order accuracy in space (at steady state) for the region $[g_1, g_4]$

$$\beta(g) = f_1 \frac{(g - g_2)(g - g_3)(g - g_4)}{(g_1 - g_2)(g_1 - g_3)(g_1 - g_4)} + f_2 \frac{(g - g_1)(g - g_3)(g - g_4)}{(g_2 - g_1)(g_2 - g_3)(g_2 - g_4)} + f_3 \frac{(g - g_1)(g - g_2)(g - g_4)}{(g_3 - g_1)(g_3 - g_2)(g_3 - g_4)} + f_4 \frac{(g - g_1)(g - g_2)(g - g_3)}{(g_4 - g_1)(g_4 - g_2)(g_4 - g_3)} \quad [33]$$

Due to the definition of f, $\partial f(g)/\partial g = \theta(g)$ and $\partial^2 f(g)/\partial g^2 = \partial \theta(g)/\partial g$. Hence, $\partial^2 \beta(g)/\partial g^2 = \partial \theta(g)/\partial g + \mathcal{O}(\Delta g_x^2)$ (at steady state). This expression is given by

$$\frac{\partial^2 \beta(g)}{\partial g^2} = f_1 \frac{(6g - 2g_2 - 2g_3 - 2g_4)}{(g_1 - g_2)(g_1 - g_3)(g_1 - g_4)} + f_2 \frac{(6g - 2g_1 - 2g_3 - 2g_4)}{(g_2 - g_1)(g_2 - g_3)(g_2 - g_4)} + f_3 \frac{(6g - 2g_1 - 2g_2 - 2g_4)}{(g_3 - g_1)(g_3 - g_2)(g_3 - g_4)} + f_4 \frac{(6g - 2g_1 - 2g_2 - 2g_3)}{(g_4 - g_1)(g_4 - g_2)(g_4 - g_3)} \quad [34]$$

The potential on the surface can be treated similarly, say with a function $\gamma(g)$, analogous to $\beta(g)$, such that $\partial^2 \gamma(g)/\partial g^2 = \partial \phi_s(g)/\partial g + \mathcal{O}(\Delta g_x^2)$. Thus, the spacial derivative of either θ or ϕ_s can be approximated with second-order accuracy.

The value of $\phi(g)$ at $g \in [g_q, g_{q+1}]$ can also be approximated with second-order accuracy in space using a linear interpolation

$$\theta_{\text{int}}(g) = \hat{\theta}_q \frac{(g - g_{q+1})}{(g_q - g_{q+1})} + \hat{\theta}_{q+1} \frac{(g - g_q)}{(g_{q+1} - g_q)} \quad [35]$$

Now, $\hat{M}_{\text{q+1/2}}$ across the boundary from q to $q + 1$ is expressed with $\mathcal{O}(\Delta g_x^2)$ approximation error (second-order accuracy) at the steady state by evaluating at the boundary point, G

$$\hat{M}_{\text{q+1/2}} = - RTu_{\text{O}',\text{s}} \left[\frac{\partial^2 \beta(G)}{\partial g^2} \right] - z_{\text{O}',\text{s}} Fu_{\text{O}',\text{s}} [\theta_{\text{int}}(G)] \left[\frac{\partial^2 \gamma(G)}{\partial g^2} \right] \quad [36]$$

Inserting the relevant expressions and letting $\mathcal{C}_a$, $\mathcal{C}_b$, $\mathcal{C}_c$, $\mathcal{C}_d$, $\mathcal{C}_e$, $\mathcal{H}_a$, and $\mathcal{H}_b$ be coefficients determined after substitution of G for g and some algebraic manipulation

$$\hat{M}^{n+1}_{q+1/2} = - RTu_{\text{O}',\text{s}} [(\mathcal{C}_a + \mathcal{C}_b + \mathcal{C}_d)\hat{\theta}^{n+1}_{q} + (\mathcal{C}_c + \mathcal{C}_e)\hat{\theta}^{n+1}_{q+1} + \mathcal{C}_e \hat{\theta}^{n+1}_{q+2}] - z_{\text{O}',\text{s}} Fu_{\text{O}',\text{s}} [\mathcal{H}_a \hat{\theta}^{n+1}_{q} + \mathcal{H}_b \hat{\theta}^{n+1}_{q+1}][(\mathcal{C}_a + \mathcal{C}_b + \mathcal{C}_d)\hat{\phi}^{n+1}_{\text{s},q} + (\mathcal{C}_c + \mathcal{C}_e)\hat{\phi}^{n+1}_{\text{s},q+1} + \mathcal{C}_e \hat{\phi}^{n+1}_{\text{s},q+2}] \quad [37]$$

This equation is used for the right boundary of cell q and the left boundary of cell $q + 1$ in conjunction with the backward Euler time discretization, Eq. 30. All fluxes are linked by Eq. 30 and solved iteratively using the line-by-line method with a tridiagonal matrix, where θ is computed implicitly. The surface potential, ϕ_s is updated at every step using Eq. 21. The tri-diagonal structure of the matrix can be preserved if the "extra" terms are treated as explicit and their value from the previous iteration is used (e.g., for cell q, the diffusive $\hat{\theta}^{n+1}_{q+2}$ term does not fit in the tri-diagonal band). This treatment of the corner preserves second-order special accuracy over the entire surface.

A zero-flux boundary condition is imposed at the endpoint adjacent to the insulator. At the TPB endpoint, the boundary condition is governed by the flux due to the TPB reaction, adsorption, and incorporation reactions. Holes created by the summation of these reactions are injected into the MIEC cell adjacent to the TPB, while vacancies consumed originate from the adjacent electrolyte cell (Fig. 2c).

The time step used was 1×10^{-6} s, and the iterations ceased when the change in the local solution was at most 0.00001%.

Parameters.— The preliminary results reported in this paper are for the specific composition $La_{0.80}Sr_{0.20}MnO_{3\pm\delta}$ (LSM20), though the model may be applied to other materials with the appropriate choice of parameters. The values chosen for this case are listed in Table I. Two new parameters, k^0_{tpb} and $u_{\text{O}',\text{s}}$, are required in addition

Table I. Parameter values at T = 1023 K.

Parameter	Value	Units	Reference
k^0_{tpb}	1.0×10^{-11} to 10^{-12}	mol/(m s)	—
k^0_{ads}	1.0	mol/(m^2 s)	—
k^0_{inc}	6.5×10^{-7}	mol/(m^2 s)	25 and 43
k^0_v	9.0×10^{-4}	mol/(m^2 s)	—
$u_{O',s}$	1.0×10^{-12}	mol m^2/(J s)	—
$u_{v,m}$	2.6×10^{-14}	mol m^2/(J s)	25 and 44
$u_{v,e}$	5.8×10^{-14}	mol m^2/(J s)	25 and 45
$u_{h,m}$	1.4×10^{-12}	mol m^2/(J s)	25 and 45
θ_0	2.0×10^{-3}	—	36
Γ	1.0×10^{-6}	mol/m^2	35 and 36
$c^0_{v,m}$	1.4×10^{-5}	mol/m^3	34
$c^0_{h,m}$	8.2×10^{3}	mol/m^3	34
$\rho_{b,m}$	-7.9×10^{8}	C/m^3	—
$\rho_{b,e}$	-9.7×10^{7}	C/m^3	—

to those from the thin-film model, of which several take on increased importance: k^0_{ads}, θ_0, and Γ. The choice of parameters assumes a temperature of 1023 K.

A recently developed refined bulk defect model[34] for LSM was used to determine the equilibrium bulk concentration of holes and vacancies, $c^0_{v,m}$ and $c^0_{h,m}$, respectively, in the MIEC. From these values, $\rho_{b,m}$ was calculated using the electroneutrality equation, Eq. 6.

A quantum chemical modeling study found that Mn sites on the surface may be preferential locations for oxygen adsorption onto $LaMnO_3$.[35] Thus, the value chosen for Γ is in rough agreement with the number of Mn sites expected on an exposed $LaMnO_3$-type perovskite. This number is close to a standard assumption in this type of analysis for perovskite surfaces,[36] as is the value chosen for θ_0.

Reliable approximations for several of the parameters, specifically k^0_{ads}, k^0_{tpb}, and $u_{O',s}$, were not found after a search of the literature. The parameter k^0_{ads} had been previously set sufficiently high so as to not limit the response of the thin film.[25] This value was used in this paper because it yielded the expected qualitative response, though k^0_{ads} does affect the TPB reaction and surface transport. For k^0_{tpb}, the value was set sufficiently low to avoid completely dominating the response of the electrode but high enough so that the TPB reaction could be detected under the right circumstances. The value chosen for $u_{O',s}$ was higher than some estimates used in other works[23,36] but was set so that the qualitative features of thin film and patterned electrode response from the literature were replicated. To the authors' knowledge, no accepted value for oxygen-surface mobility on a $LaMnO_3$-type perovskite has been reported in the literature. A seemingly acceptable range of values for each of these parameters was determined and is presented in the next section. Accurate determination of these parameters is beyond the scope of this paper but will be the subject of future work.

Results and Discussion

Parameters.— The reaction rates from the 2D simulation may be summed over the model domain and adjusted by the Faraday constant to obtain current, which can be expressed with the units A/m, where the m^{-1} refers to the current per unit length of patterned electrode. The current resulting from the TPB and bulk processes as well as the sum of the two is given in Fig. 3a-c for varying surface parameters.

The choice of k^0_{tpb} is shown to have a dramatic impact upon the overall electrochemical performance in Fig. 3a. If k^0_{tpb} is low, the TPB current is insignificant and the bulk processes dominate the electrochemical response. If it is high, the TPB current overshadows the bulk current. For this paper, k^0_{tpb} values have been chosen in the moderate region of 10^{-11} to 10^{-12} mol/(m s) so that under some

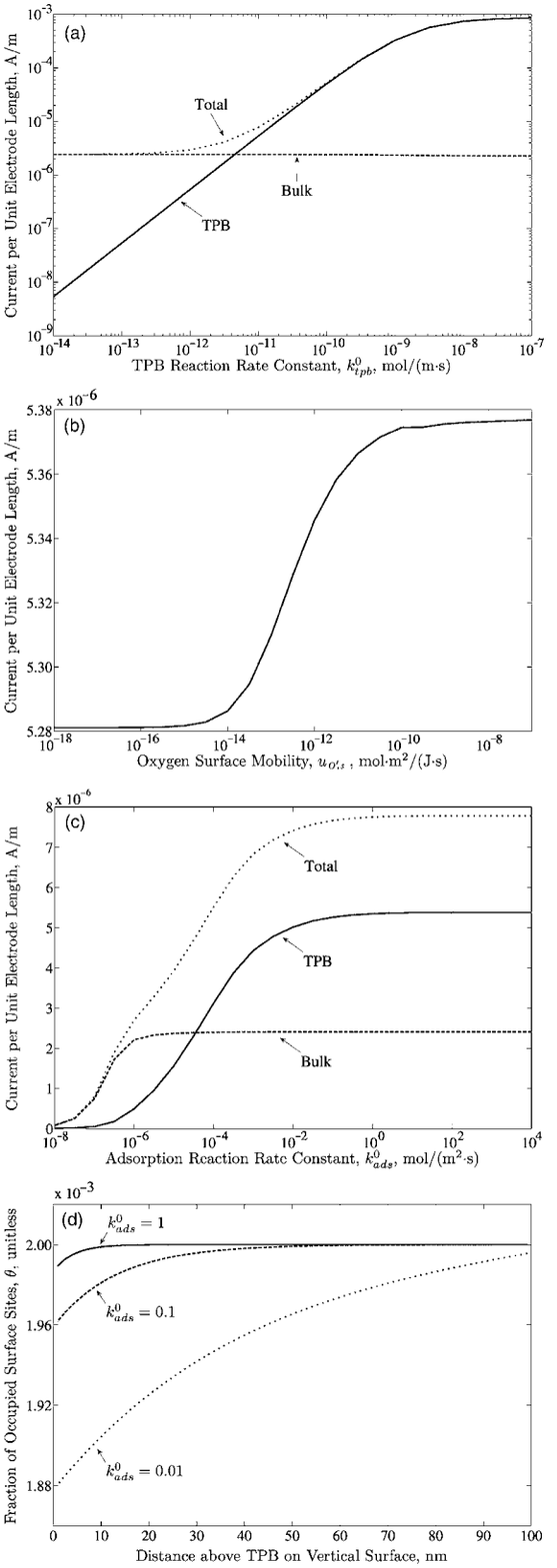

Figure 3. Dependence of electrochemical response upon surface parameters: effect of varying (a) k^0_{tpb}, (b) $u_{o',s}$ and (c) k^0_{ads}. TPB current (solid), bulk current (long dashes), and total current (short dashes). (d) Dependence of surface concentration (fraction of occupied surface sites, θ) upon value of k^0_{ads}. k^0_{ads} = 1 (solid), 0.1 (long dashes), and 0.01 mol/(m^2 s) (short dashes). Extrinsic factors: active width = 48 μm (see Fig. 1), thickness = 100 nm, applied voltage = −0.100 V. Except for (a), $k^0_{tpb} = 10^{-11}$ mol/(m s).

conditions the TPB might determine performance but under others the bulk might determine performance, as observed in porous[37-40] vs patterned[4,10] electrode experiments, respectively.

When $u_{O',s}$ is varied (Fig. 3b), low values lead to elimination of surface transport and the TPB reaction is supplied only by adsorption. High values lead to the TPB reaction being supplied by both adsorption and surface transport, evenually causing surface transport to reach a limit. The value of $u_{O',s}$ has been chosen in the middle region for this paper.

The adsorption reaction is responsible for supplying O'_{ads} to the surface, and therefore it supplies both the TPB and the bulk incorporation reactions. At low values of k^0_{ads} (Fig. 3c), it limits both. As it increases, there is a region where it limits only the TPB reaction. After increasing further, it is nonlimiting to either one. The value assigned to k^0_{ads} in this paper was on the high end of the TPB-limiting region.

The effect of k^0_{ads} upon the surface concentration is given in Fig. 3d. As k^0_{ads} decreases, the TPB reaction is directly supplied with less oxygen and the importance of suface transport is increased. As a result, θ at the TPB endpoint decreases and the depletion distance on the surface increases in length.

Changing the parameters causes effects that overlap. For instance, decreasing k^0_{ads} may increase the depletion distance, but decreasing $u_{O',s}$ causes the opposite effect. The range selected for the parameters allows qualitative agreement with experimental result, which is discussed in the next sections.

Electrode geometry and applied voltage.— The currents resulting from varying electrode width, thickness, and applied potential are given in Fig. 4-6, respectively. Each plot is shown with two different (moderate) values of k^0_{tpb}.

From Fig. 4, the TPB current is relatively constant while the bulk contribution varies almost linearly with active width. A correlation between width and active area may be made due to the specific geometry of the patterned electrode (Fig. 1), and thus the bulk contribution scales directly with active area while the TPB contribution is relatively constant. The total current approaches the TPB current as the width approaches zero. This correlation is in qualitative agreement with Brichzin et al.[4] and Ioroi et al.,[10] who determined that electrode resistance (R_{el}) correlated directly with area.

The TPB current can range from a dominant to miniscule portion of the total current based upon the value assigned to k^0_{tpb} as well as the geometry. In Fig. 4a, $k^0_{tpb} = 10^{-11}$ mol/(m s), which makes the TPB current greater than the bulk current for almost all widths shown. However, in Fig. 4b, $k^0_{tpb} = 10^{-12}$ mol/(m s), so the TPB current is greater only at small widths. As the electrode width (area) decreases, the TPB contributes a greater fraction of the total current.

Brichzin et al.[4] and Ioroi et al.[10] both concluded that, for patterned electrodes, the TPB contribution was insignificant compared to the bulk contribution and used the direct correlation of R_{el} vs electrode area as proof. However, Brichzin et al. did not consider the intercept of R_{el} at zero area. If the line is extrapolated to zero area, some measure of TPB resistance may be obtained. Also, Ioroi et al.'s experimental design was heavily weighted toward area-dependent processes (area to TPB length ratio on the order of ~1000 $\mu m^2/\mu m$ compared to 0.5–128 $\mu m^2/\mu m$ in this paper). Had any defects (such as nanoporosity, cracks, etc.) been present in that film, it is not unreasonable for the TPB contribution from the well-defined line to have been drowned out by the combination of TPB contribution arising from these defects and a large bulk contribution. Others have concluded that the TPB reaction can in fact be detected with carefully controlled experimental geometries.[23,24,41]

Next, the effect of film thickness is shown in Fig. 5. The total contribution of the TPB is again highly dependent upon the magnitude of k^0_{tpb} but is relatively constant with thickness. In contrast, the bulk current is governed by electrode resistance that is directly proportional to the thickness, leading to the linear trend in the log–log plot. This result is in agreement with experimental results.[8,10] Given

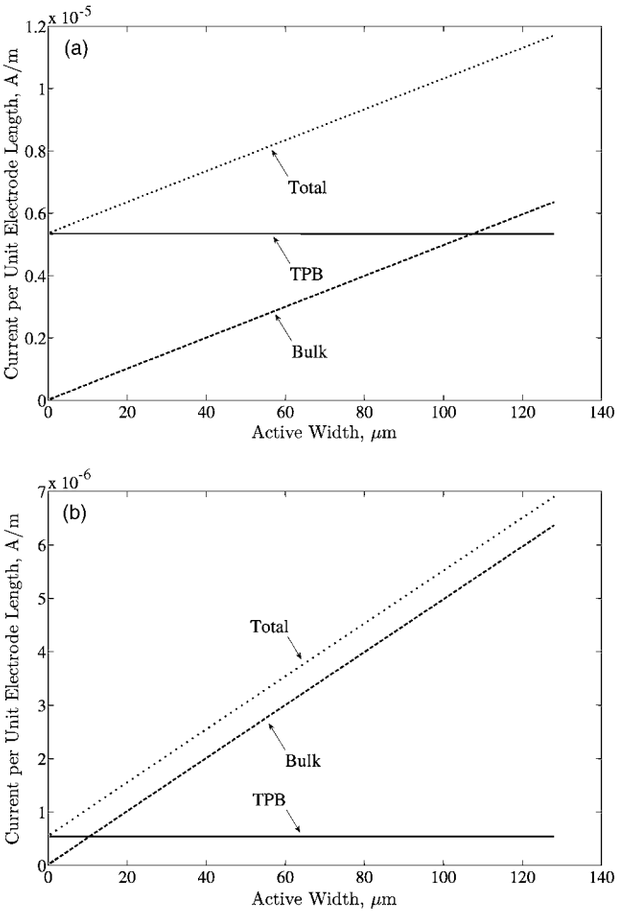

Figure 4. Current per unit electrode length vs active film width for film thickness of 100 nm and applied voltage of −0.100 V: (a) $k^0_{tpb} = 10^{-11}$ and (b) $k^0_{tpb} = 10^{-12}$ mol/(m s). TPB current (solid), bulk current (long dashes), and total current (short dashes).

the proper value of k^0_{tpb}, the total current can be dominated by the TPB at high thickness but dominated by the bulk at low thickness.

The dependence of current upon applied voltage is given in Fig. 6. At moderate polarizations, the TPB contribution can dominate given a high k^0_{tpb} (Fig. 6a), while for smaller k^0_{tpb} it makes up a large portion of the overall current as well (Fig. 6b). As cathodic polarization increases, the bulk current rises at a greater rate than the TPB current. At the most extreme cathodic polarizations, the bulk current is dominant, reflecting the trend toward activation of the bulk due to significant change in stoichiometry of the MIEC.[41,42] The shape of the curve is a qualitative match to experimental thin film[7-9,11,17,20] and patterned electrode[10] data.

Based upon these results, it is proposed that the TPB contribution to the overall current can be determined and its kinetics examined by designing patterned electrodes that favor the TPB process. The electrode design may be of the form shown in Fig. 1, with essential features that include large thickness, a range of active area, and low polarization. These features are in agreement with predictions made by other authors.[4,23] The contribution of the TPB may then be isolated by interpolating the zero-area intercept using patterned electrodes of different active area. Such experiments will be the subject of future work.

Sheet resistance.— It has been experimentally documented[4,15] that sheet resistance is noticeable in LSM thin film and patterned electrodes given certain combinations of electrode geometry and applied voltage. The external factors that produced Fig. 4-6 were

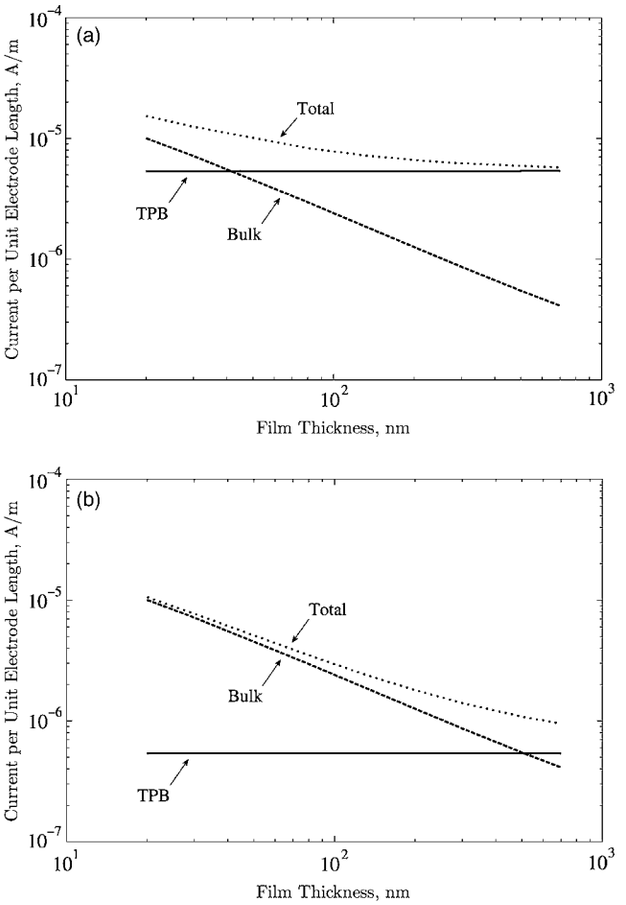

Figure 5. Current per unit electrode length vs film thickness for active width of 48 μm and applied voltage of −0.100 V: (a) $k^0_{tpb} = 10^{-11}$ and (b) $k^0_{tpb} = 10^{-12}$ mol/(m s). TPB current (solid), bulk current (long dashes), and total current (short dashes).

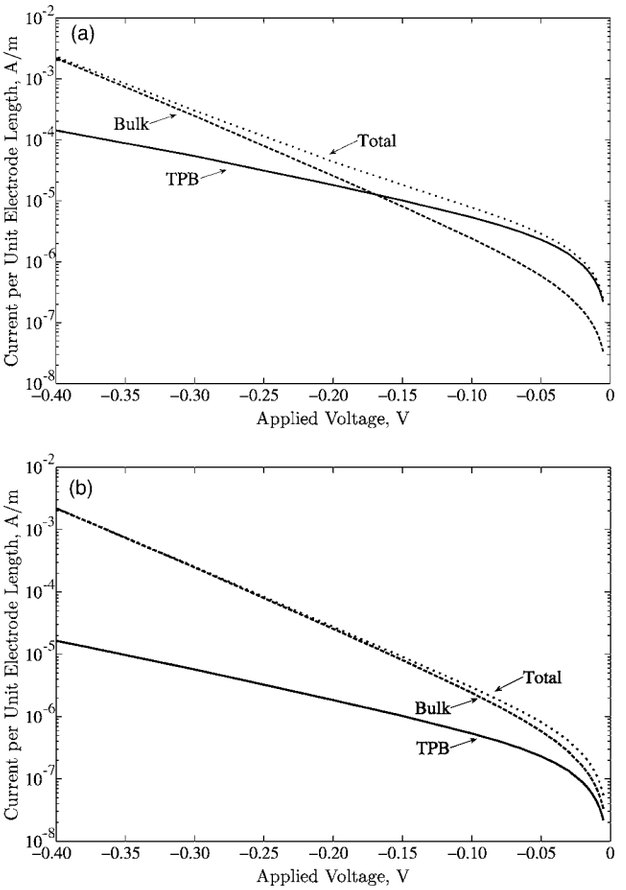

Figure 6. Current per unit electrode length vs applied voltage for active width of 48 μm and film thickness of 100 nm: (a) $k^0_{tpb} = 10^{-11}$ and (b) $k^0_{tpb} = 10^{-12}$ mol/(m s). TPB current (solid), bulk current (long dashes), and total current (short dashes).

specified in order to show an ideal response under the given set of material parameters, but the model can also predict behavior impacted substantially by sheet resistance (Fig. 7 and 8).

In Fig. 7, for active width ~400 μm and applied voltage of −0.100 V, the aspect ratio becomes more extreme as thickness decreases. As a consequence, the total current deviates from ideality due to the deactivation of surfaces far away from the current collector. This deviation is noticeable under the given parameterization when the mobility of vacancies, $u_{v,m}$, is increased; at sufficiently extreme aspect ratios and $u_{v,m}$, the current reaches a maximum and then decreases as film thickness decreases. Therefore, the maximum current does not correspond to the thinnest film. This general type of behavior was observed experimentally by Koep et al.[15] Though the patterned electrode geometry, applied voltage, and parameterization used here do not yield an exact match to Koep et al.'s observations, they do yield behavior that is qualitatively similar. It is possible that an exact match might be obtained given the correct parameterization.

Figure 8 shows how the TPB current is specifically affected by sheet resistance. At moderate aspect ratios, the reaction rate is relatively constant, but as the aspect ratio becomes more distorted by decreasing film thickness, the TPB reaction is deactivated and the current is decreased. This deactivation is the direct result of the potential of the MIEC deviating increasingly from the applied voltage, which decreases the potential difference between the electrolyte and both the MIEC and the surface (χ_{em} and χ_{es}, respectively), resulting in a decreased reaction rate. In Fig. 8a, the potential vs horizontal distance (from left to right across the electrode, where the TPB potential is at 800 μm) is shown for different film thicknesses.

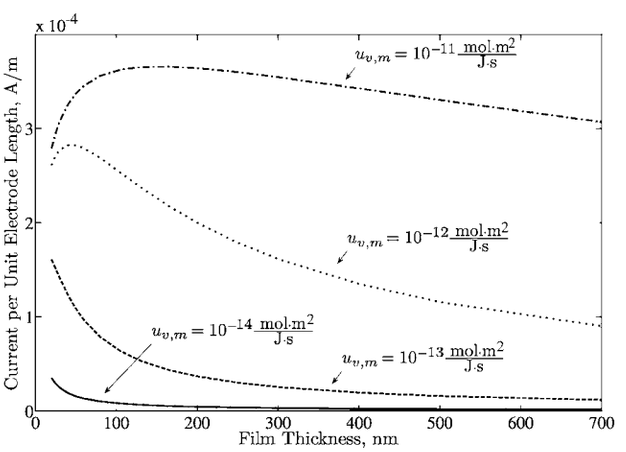

Figure 7. Total current per unit electrode length vs film thickness for different values of $u_{v,m}$. As $u_{v,m}$ increases, the effect of sheet resistance is increased, which is reflected in the decrease in current with decreasing thickness for low thicknesses. Active width ~400 μm, $k^0_{tpb} = 10^{-12}$, applied voltage = −0.100 V, and $u_{v,m} = 10^{-14}$ mol m^2/(J s) (solid), 10^{-13} (long dashes), 10^{-12} (short dashes), and 10^{-11} (uneven dashes).

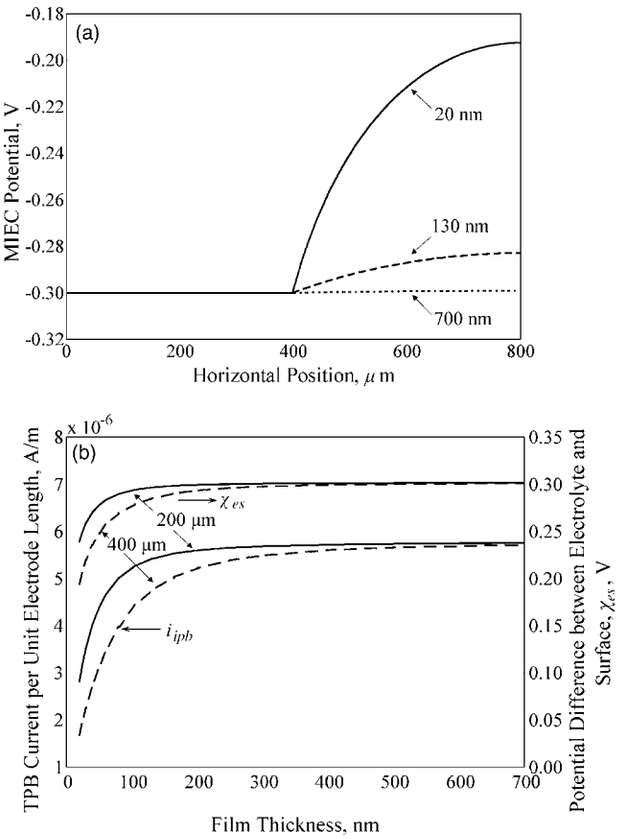

Figure 8. Plots showing the deactivation of the TPB reaction at extreme aspect ratios with $k^0_{tpb} = 10^{-12}$ mol/(m s) and applied voltage of −0.300 V. (a) Potential of the MIEC is shown for films with active width ~400 μm and different thickness as a function of horizontal distance from left to right across the 2D model domain. Potential is constant in the dead area under the current collector but rises parabolically with distance away from the current collector. The potential of the MIEC at the TPB is located at 800 μm. Film thickness: 20 (solid), 130 (long dashes), and 700 nm (short dashes). (b) The TPB current per unit electrode length, i_{tpb}, and the potential difference between the electrolyte and the surface, χ_{es}, are plotted together. The lower set of curves corresponds to i_{tpb} (referred to left axis), while the upper set of curves corresponds to χ_{es} (referred to right axis). Active width ~200 (solid) and ~400 μm (long dashes).

The deviation is approximately parabolic with distance from the current collector, and as the aspect ratio becomes more extreme, the deviation increases. The TPB current, i_{tpb}, and χ_{es} are plotted in Fig. 8b on separate axes.

It is an important observation that the TPB current trends oppositely with respect to film thickness than the bulk current. As thickness decreases, the bulk current usually increases faster than sheet resistance can limit it, so the net result is that current increases, though not always ideally. However, because the TPB reaction is not limited by bulk transport, the decreasing thickness does not ameliorate transport to or from the reaction site. Thus, the TPB reaction depends only upon the potential difference between the MIEC and the electrolyte at the TPB, which deviates from ideal as film thickness decreases.

Conclusion

A 2D numerical model of an MIEC thin-film electrode has been extended to include a TPB and the accompanying surface transport. This addition enables the modeling of the electrochemical and transport response of a true patterned, multidimensional MIEC electrode. While the exact values for the parameters are yet to be determined, the model replicates qualitatively the results from experimental studies of patterned LSM, including the effect of electrode geometry (width and thickness), testing conditions (applied voltage), and sheet resistance. The rate of the TPB reaction was shown to be relatively constant vs film width and thickness when the effect of sheet resistance was insignificant, though it was predicted to decrease with the effect of sheet resistance caused by extreme film aspect ratios. A possible method of experimentally measuring some key kinetic features was proposed, including separating the TPB and bulk reaction rates. To determine TPB reaction kinetics, for example, a specific patterned electrode geometry is suggested, including large film thickness, small area, and low polarization.

The development of these new model features leads to the potential for quantitative estimates of phenomenological parameters of electrode materials by rigorous comparison to experiment and for prediction of cell performance. Furthermore, this approach can also be used to directly link the predictions from first principles-based calculations with materials performance as measured in test cells of well-controlled geometries, filling a vital role in multiscale modelling and simulation of SOFC cathodes. If adapted for an unstructured mesh, it has the potential to predict the effect of arbitrary material geometry on chemical, catalytic, and electrochemical properties of SOFC cathodes. Future work will concentrate on these areas.

Acknowledgments

This work was supported by a National Science Foundation graduate research fellowship, by the U.S. DOE University Coal Research Program under grant no. DEFG26-06NT42735, by DOE Basic Energy Science under grant no. DE-FG02-06ER15837, and by the National Science Foundation under grant no. DMS-0511815.

Georgia Institute of Technology assisted in meeting the publication costs of this article.

List of Symbols

A	area of capacitor plates, m^2
a_k	activity of species k, unitless
$a_{k,e}$	activity of species k in the electrolyte, unitless
$a_{k,m}$	activity of species k in the MIEC, unitless
c_k	concentration of species k, mol/m^3
$c_{h,m}$	concentration of electron holes in the MIEC, mol/m^3
$c_{Mn,m}$	concentration of regular manganese lattice sites in the MIEC, mol/m^3
$c_{O,e}$	concentration of regular oxygen lattice sites in the electrolyte, mol/m^3
$c_{O',s}$	concentration of adsorbed oxygen on the surface, mol/m^2
$c_{v,e}$	concentration of oxygen vacancies in the electrolyte, mol/m^3
d, d_{ms}	distance of surface charge separation, m
$\mathcal{C}_a$, $\mathcal{C}_b$, $\mathcal{C}_c$, $\mathcal{C}_d$, $\mathcal{C}_e$, $\mathcal{H}_a$, and $\mathcal{H}_b$	geometric coefficients for surface flux equation
F	Faraday's constant
$f(x)$	integral of θ on surface
G_k	homogeneous generation rate of species k, $mol/(m^3\ s)$
ΔG^0_A	standard activation energy for transition state A, J/mol
g	surface location, m
Δg	surface cell size, m
$h^{\cdot}$	electron hole
$h^{\cdot}_m$	electron hole in the MIEC
h_P	Planck's constant
k	reaction rate constant, s^{-1}
k'	reaction rate constant incorporating constant terms, s^{-1}
k''	reaction rate constant incorporating constant terms and activity coefficients, s^{-1}
k'''	reaction rate constant adjusted for concentration and geometry, mol/(m·s)
k^0_{ads}	reaction rate constant for adsorption reaction, $mol/(m^3\ s)$
k^0_{inc}	reaction rate constant for incorporation reaction, $mol/(m^3\ s)$
k^0_{tpb}	reaction rate constant for TPB reaction, mol/(m s)
k^0_v	reaction rate constant for vacancy transfer from electrolyte to MIEC, $mol/(m^2\ s)$
k_B	Boltzmann's constant

$\hat{M}_k$	surface flux of species k normalized by Γ, m/s
$\vec{N}_k$	flux of species k, mol/(m^2 s)
O_O^x	oxygen ion in a regular oxygen site in the MIEC or the electrolyte
$O_{O,e}^x$	oxygen ion in a regular oxygen site in the electrolyte
$O_{O,m}^x$	oxygen ion in a regular oxygen site in the MIEC
O'_{ads}	adsorbed oxygen (partially reduced)
Q	total charge on capacitor plate, C
R	universal gas constant, J/(mol K)
r_{ads}	reaction rate for adsorption reaction, mol/(m^2 s)
r_{inc}	reaction rate for incorporation reaction, mol/(m^2 s)
r_{tpb}	reaction rate for TPB reaction, mol/(m s)
r_v	reaction rate for vacancy transfer from electrolyte to MIEC, mol/(m^2 s)
s	vacant surface site
T	absolute temperature, K
t	time, s
u_k	absolute mobility of species k, mol · m^2/(J s)
$V_O^{\cdot\cdot}$	oxygen vacancy
$V_{O,e}^{\cdot\cdot}$	oxygen vacancy in the electrolyte
$V_{O,m}^{\cdot\cdot}$	oxygen vacancy in the MIEC
z_k	charge number of species k
α	transfer coefficient, unitless
$\beta(g)$	interpolation function of $f(x)$
Γ	density of surface sites, mol/m^2
$\gamma(g)$	interpolation function related to surface potential, analogous to $\beta(g)$
ε_0	permittivity of free space
θ	fraction of occupied surface sites, unitless
μ_k	chemical potential of species k, J/mol
$\mu_{k,e}$	chemical potential of species k in the electrolyte, J/mol
$\mu_{k,m}$	chemical potential of species k in the MIEC, J/mol
$\mu_{k,s}$	chemical potential of species k on surface, J/mol
$\tilde{\mu}_k$	electrochemical potential of species k, J/mol
ρ_b	background charge density, C/m^3
$\rho_{b,e}$	background charge density in the electrolyte, C/m^3
$\rho_{b,m}$	background charge density in the MIEC, C/m^3
ϕ	electrostatic potential, V
κ	transmission coefficient, unitless
χ	difference in electrostatic potential across interface, V
χ_{em}	difference in electrostatic potential across electrolyte/MIEC interface, V
χ_{es}	difference in electrostatic potential between electrolyte and surface, V
χ_{ms}	difference in electrostatic potential between MIEC and surface, V
$\Delta\chi$	variation of χ from equilibrium value

Superscript

0	refers to the equilibrium value
n	quantity at time step n
n + 1	quantity at time step n + 1

Subscript

0	refers to the equilibrium value
ads	adsorbed species
A	refers to the transition state
e	quantity in the electrolyte
elect.	only the electrical component should be considered
em	quantity in the MIEC subtracted from quantity in the electrolyte
es	quantity on the surface subtracted from quantity in the electrolyte
h	electron holes
I	initial state
II	final state
int	interpolated value
k	species k
m	quantity in the MIEC
ms	quantity on the surface subtracted from quantity in the MIEC
O'	adsorbed oxygen species
p	surface cell index
q	surface cell index
s	quantity on the surface
tpb	triple phase boundary between the electrolyte, the MIEC, and air
v	oxygen vacancies
x	horizontal direction
y	vertical direction

References

1. B. C. Steele, *Solid State Ionics*, **86–88**, 1223 (1996).
2. M. Liu, *J. Electrochem. Soc.*, **145**, 142 (1998).
3. F. S. Baumann, J. Fleig, H.-U. Habermeier, and J. Maier, *Solid State Ionics*, **177**, 1071 (2006).
4. V. Brichzin, J. Fleig, H.-U. Habermeier, G. Cristiani, and J. Maier, *Solid State Ionics*, **152–153**, 499 (2002).
5. V. Brichzin, J. Fleig, H. Habermeier, and J. Maier, *Electrochem. Solid-State Lett.*, **3**, 403 (2000).
6. A. Endo, H. Fukunaga, C. Wen, and K. Yamada, *Solid State Ionics*, **135**, 353 (2000).
7. A. Endo, S. Wada, C. Wen, H. Komiyama, and K. Yamada, *J. Electrochem. Soc.*, **145**, L35 (1998).
8. A. Endo, M. Ihara, H. Komiyama, and K. Yamada, *Solid State Ionics*, **86–88**, 1191 (1996).
9. N. Imanishi, T. Matsumura, Y. Sumiya, K. Yoshimura, A. Hirano, Y. Takeda, D. Mori, and R. Kanno, *Solid State Ionics*, **174**, 245 (2004).
10. T. Ioroi, T. Hara, Y. Uchimoto, Z. Ogumi, and Z.-I. Takehara, *J. Electrochem. Soc.*, **144**, 1362 (1997).
11. T. Ioroi, T. Hara, Y. Uchimoto, Z. Ogumi, and Z.-I. Takehara, *J. Electrochem. Soc.*, **145**, 1999 (1998).
12. T. Kawada, J. Suzuki, M. Sase, A. Kaimai, K. Yashiro, Y. Nigara, J. Mizusaki, K. Kawamura, and H. Yugami, *J. Electrochem. Soc.*, **149**, E252 (2002).
13. T. Kawada, K. Masuda, J. Suzuki, A. Kaimai, K. Kawamura, Y. Nigara, J. Mizusaki, H. Yugami, H. Arashi, N. Sakai et al., *Solid State Ionics*, **121**, 271 (1999).
14. E. Koep, C. Compson, M. Liu, and Z. Zhou, *Solid State Ionics*, **176**, 1 (2005).
15. E. Koep, D. S. Mebane, R. Das, C. Compson, and M. Liu, *Electrochem. Solid-State Lett.*, **8**, A592 (2005).
16. C. Mims, N. Joos, P. v. d. Heide, A. Jacobson, C. Chen, C. Chu, B. Kim, and S. Perry, *Electrochem. Solid-State Lett.*, **3**, 59 (2000).
17. J. Mizusaki, T. Saito, and H. Tagawa, *J. Electrochem. Soc.*, **143**, 3065 (1996).
18. D. Mori, H. Oka, Y. Suzuki, N. Sonoyama, A. Yamada, R. Kanno, Y. Sumiya, N. Imanishi, and Y. Takeda, *Solid State Ionics*, **177**, 535 (2006).
19. A. Ringuedé and J. Fouletier, *Solid State Ionics*, **139**, 167 (2001).
20. Y. Takeda, R. Kanno, M. Noda, Y. Tomida, and O. Yamamoto, *J. Electrochem. Soc.*, **134**, 2656 (1987).
21. Y. Yang, C. Chen, S. Chen, C. Chu, and A. Jacobson, *J. Electrochem. Soc.*, **147**, 4001 (2000).
22. Y. L. Yang, A. Jacobson, C. Chen, G. Luo, K. Ross, and C. Chu, *Appl. Phys. Lett.*, **79**, 776 (2001).
23. G. la O', B. Yildiz, S. McEuen, and Y. Shao-Horn, *J. Electrochem. Soc.*, **154**, B427 (2007).
24. R. Radhakrishnan, A. V. Virkar, and S. Singhal, *J. Electrochem. Soc.*, **152**, A210 (2005).
25. D. S. Mebane, Y. Liu, and M. Liu, *J. Electrochem. Soc.*, **154**, A421 (2007).
26. D. S. Mebane and M. Liu, *J. Solid State Electrochem.*, **10**, 575 (2006).
27. D. S. Mebane and M. Liu, *J. Solid State Electrochem.*, **11**, 448 (2007).
28. S. W. Feldberg, *J. Electroanal. Chem. Interfacial Electrochem.*, **127**, 1 (1981).
29. T. Joslin and D. Pletcher, *J. Electroanal. Chem. Interfacial Electrochem.*, **49**, 171 (1974).
30. D. Britz, *Digital Simulation in Electrochemistry*, 3rd ed., Springer, New York (2005).
31. A. Harten, B. Engquist, S. Osher, and S. R. Chakravarthy, *J. Comput. Phys.*, **71**, 231 (1987).
32. B. van Leer and S. Nomura, AIAA Paper 2005-5108, in *Collection of Technical Papers—AIAA 17th Computational Fluid Dynamics Conference*, p. 1 (2005).
33. B. van Leer, M. Lo, and M. Van Raalte, AIAA Paper 2007-4083, in *Collection of Technical Papers—AIAA 18th Computational Fluid Dynamics Conference*, p. 763 (2007).
34. D. S. Mebane, Y. Liu, and M. Liu, *Solid State Ionics*, **178**, 1950 (2008).
35. Y. Choi, D. S. Mebane, M. Lin, and M. Liu, *Chem. Mater.*, **178**, 1950 (2008).
36. A. M. Svensson, S. Sunde, and K. Nisancioglu, *J. Electrochem. Soc.*, **144**, 2719 (1997).
37. J. Mizusaki, H. Tagawa, K. Tsuneyoshi, and A. Sawata, *J. Electrochem. Soc.*, **138**, 1867 (1991).
38. K. Sasaki, J.-P. Wurth, R. Gschwend, M. Gödickemeier, and L. Gauckler, *J. Electrochem. Soc.*, **143**, 530 (1996).
39. H. Fukunaga, M. Ihara, K. Sakaki, and K. Yamada, *Solid State Ionics*, **86–88**, 1179 (1996).
40. M. Østergård, C. Clausen, C. Bagger, and M. Mogensen, *Electrochim. Acta*, **40**, 1971 (1995).
41. E. Siebert, A. Hammouche, and M. Kleitz, *Electrochim. Acta*, **40**, 1741 (1995).
42. H. Lauret and A. Hammou, *J. Eur. Ceram. Soc.*, **16**, 447 (1996).
43. R. De Souza and J. Kilner, *Solid State Ionics*, **126**, 153 (1999).
44. R. De Souza and J. Kilner, *Solid State Ionics*, **106**, 175 (1998).
45. N. Minh and T. Takahashi, *Science and Technology of Ceramic Fuel Cells*, Elsevier, Amsterdam (1995).